1994ApJ...431..188V

THE ASTROPHYSICAL JOURNAL, 431:188–200, 1994 August 10
© 1994. The American Astronomical Society. All rights reserved. Printed in U.S.A.

A STUDY OF X-RAY AND INFRARED EMISSIONS FROM DUSTY NONRADIATIVE SHOCK WAVES

OLAF VANCURA,[1] JOHN C. RAYMOND,[1] ELI DWEK,[2] WILLIAM P. BLAIR,[3]
KNOX S. LONG,[3,4] AND SCOTT FOSTER[5]
Received 1993 October 7; accepted 1994 February 10

ABSTRACT

We have constructed models that predict the dynamic evolution and infrared (IR) emission of grains behind nonradiative shock waves. We present a self-consistent treatment of the effect of grain destruction and heating on the ionization structure and X-ray emission of the postshock gas. Incorporating thermal sputtering, collisional heating, and deceleration of grains in the postshock flow, we predict the IR and X-ray fluxes from the dusty plasma as a function of swept-up column density. Heavy elements such as C, O, Mg, S, Si, and Fe are initially depleted from the gas phase but are gradually returned as the grains are destroyed. The injected neutral atoms require some time to "catch up" with the ionization state of the ambient gas. The nonequilibrium ionization state and gradient in elemental abundances in the postshock flow produces characteristic X-ray signatures that can be related to the age of the shock and amount of grain destruction. We study the effects of preshock density and shock velocity on the X-ray and IR emission from the shock. We show that the effects of grain destruction on the X-ray spectra of shock waves are substantial. In particular, temperatures derived from X-ray spectra of middle-aged remnants are likely to be overestimated by $\sim 15\%$ if cosmic abundances are assumed. Due to the long timescale for grain destruction in X-ray gases over a wide range of temperatures, we suggest that future X-ray spectral studies of supernova remnants be based on depleted abundances instead of cosmic abundances. Our model predictions agree reasonably well with *IRAS* and *Einstein* IPC observations of the Cygnus Loop.

Subject headings: dust, extinction — ISM: abundances — ISM: individual (Cygnus Loop) — shock waves — supernova remnants

1. INTRODUCTION

Shock waves in supernova remnants (SNRs) provide a forum for the study of interstellar dust grain evolution in plasmas. Dust immersed in a high-temperature gas is both heated and destroyed by collisions between the gas and grains. Heating leads to thermal IR emission from the dust, while the destruction of dust in the postshock flow of shock waves leads to enhanced gas emissivities by liberating many elements such as C, Si, Mg, and Fe which are depleted onto grains in the ambient ISM.

The evolution of grains in hot plasmas has been studied in considerable detail (see review by Dwek & Arendt 1992). Theoretical models have been used to predict IR and X-ray emissions from evolving grains immersed in gases with varying physical parameters. Dwek (1986, 1987) calculated several IR diagnostics for dusty plasmas, deriving equilibrium dust temperatures, and discussing the effects of stochastic heating on grains. Seab (1987) and Tielens et al. (1994) presented the thermal sputtering destruction rate of dust immersed in a hot gas. Itoh (1989) has discussed the effectiveness of grain destruction in enhancing X-ray emissivity.

The extension to grain evolution behind shock waves necessitates a dynamic treatment. The study of dusty shock waves divides naturally into two classes. Behind "nonradiative" shocks, where cooling has negligible impact on postshock gas dynamics, thermal sputtering plays the key role in grain disruption. On the other hand, after a shock wave becomes "radiative," with significant energy loss and subsequent temperature drop and compression, the effects of nonthermal sputtering and grain-grain collisions will dominate grain destruction. Draine (1981) presented a pioneering study of IR emission from dust behind shock waves. McKee et al. (1987) presented models of grain evolution behind radiative shocks of velocities ~ 100 km s^{-1}.

In this paper, we study the evolution of grains behind fast, nonradiative shocks. For the first time, we employ a dynamic model of the postshock region that includes grain destruction, continually updated abundances and plasma diagnostics, and grain heating and emissions. As a function of swept-up column density, we predict observable X-ray spectra and fluxes and compare cases with and without grain evolution. We also predict observable postshock IR fluxes from the continually evolving dust. We discuss our approach and assumptions in § 2. Model predictions are discussed in § 3. We compare our predictions to existing observations of the Cygnus Loop in § 4. We briefly discuss ramifications of our study in § 5 and summarize in § 6.

2. THE DUSTY SHOCK WAVE MODEL

Our approach was to develop computer code that monitors grain evolution and predicts the infrared emission from the dust under a variety of physical conditions. This grain code

[1] Harvard-Smithsonian Center for Astrophysics, 60 Garden Street, Cambridge, MA 02138.
[2] Code 685, NASA/Goddard Space Flight Center, Greenbelt, MD 20771.
[3] Center for Astrophysical Sciences, Department of Physics and Astronomy, The Johns Hopkins University, 34th and Charles Streets, Baltimore, MD 21218.
[4] Space Telescope Science Institute, 3700 San Martin Drive, Baltimore, MD 21218.
[5] Department of Astronomy, University of Maryland, College Park, MD 20742.

© American Astronomical Society • Provided by the NASA Astrophysics Data System

1994ApJ...431..188V

links with the shock wave code of Raymond (1979; see also improvements in Cox & Raymond 1985 and Long et al. 1992). The shock wave code follows the evolution of a shocked parcel of gas in the reference frame of the shock front. Step sizes of varying temporal length are used to achieve integrated fluxes and to update densities, ionic concentrations, temperatures, and emissivities in a continuous fashion. In each shock integration step, the prevailing physical conditions determine the grain destruction rate from thermal sputtering and the grain deceleration rate from thermal collisions. Given the sputtering rate, the mass loss for each type of grain is inferred, which in turn yields the relative amount of each element released into the plasma. The abundances of all elements in the gas phase are updated, as are the ionization fractions. At each step, the heating rate and total IR spectrum of the surviving grains are also determined. The IR emission in the *IRAS* 60 μm and 100 μm bandpasses is calculated using the bandpass transmissions given by Neugebauer et al. (1984). The 12 μm and 25 μm emissivities are strongly affected by stochastic (non-equilibrium) heating of small grains and will be included in a subsequent paper (Dwek et al. 1994).

2.1. *Formalism*

In general, for a spherical grain of radius a, charge Q, electric potential $U = Q/a$, and velocity V_{gr}, moving through a Maxwellian distribution of gas particles with mass m, charge q, number density n, and temperature T, the rate R of a physical process involving collisions between the grain and plasma is given by (e.g., Dwek & Arendt 1992),

$$R = \pi a^2 n \int v\left(1 - \frac{\phi}{\beta v^2}\right)\xi(v, U, \theta)dF , \tag{1a}$$

where

$$dF = 2\pi\left(\frac{\beta}{\pi}\right)^{3/2} \exp\left[-\beta(V_{gr}^2 + v^2 - 2vV_{gr}\cos\theta)\right] \times v^2 \sin\theta\, dv\, d\theta . \tag{1b}$$

The integral is taken over all incident particle velocities v and angles θ. $\phi = qU/kT$, $\beta = m/2kT$, and $\xi(v, U, \theta)$ is the quantity transferred (see below) between collisions of the grain and gas. For ξ independent of θ, equation (1) can be written as,

$$R = \pi a^2 n\left(\frac{32kT}{\pi m}\right)^{1/2}\gamma , \tag{2a}$$

where

$$\gamma = \frac{1}{2}\frac{\exp(-S^2)}{2S}\int \epsilon^{1/2}\exp(-\epsilon)\left(1 - \frac{\phi}{\epsilon}\right) \times \sinh(2S\epsilon^{1/2})\xi(\epsilon, \phi)d\epsilon . \tag{2b}$$

The integral is taken over all incident particle energies $\epsilon\ (= E/kT)$. $\xi(\epsilon, \phi)$ is equal to the θ-averaged value of $\xi(v, U, \theta)$; S^2 is equal to $mV_{gr}^2/2kT$ and is representative of the square of the ratio of grain kinetic velocity to the thermal velocity of the gas particle. Note that as $\phi \to 0$, letting $S \to 0$ recovers the familiar Maxwellian integral for γ.

2.2. *Grain Heating*

Grains are heated primarily by collisions with electrons, protons, He, and CNO nuclei. For incident particles of energy E, define σ to be the fraction of incident energy deposited into the grains upon a collision (see Dwek 1987). With this nomenclature, $\xi(\epsilon, a) = \sigma(E, a)E = \sigma(\epsilon, a)kT\epsilon$. Values for $\sigma(\epsilon, a)$ and their derivation are discussed in detail in Dwek (1987) and Dwek et al. (1994). Briefly, a grain's stopping thickness, which is proportional to its radius, is compared to the incident particle's stopping range, dependent on energy. If the incident particle's range is less than the thickness of the grain, all the energy is deposited into the grain. Otherwise, the difference is used to derive the fraction of deposited energy. The grain heating rate as a function of grain size and gas temperature was calculated by numerical integration of equations (2) and appears in Dwek et al. (1994). For $T \leq 5 \times 10^6$ K, incident particles, including electrons, are nearly 100% efficient in depositing their energy, hence $\sigma \approx 1$, and the heating rate goes as $nT^{3/2}$. For a plasma with cosmic abundances, the electron heating dominates by roughly an order of magnitude, followed by contributions from H, He, and CNO nuclei, respectively. At temperatures higher than $\sim 3 \times 10^7$ K, the electronic heating rate declines as σ falls, whereupon at $\sim 2 \times 10^8$ K, the proton and electron heating contributions are equal.

The equilibrium dust temperature is determined by equating the collisional heating rate, $H_{coll}(a, n, T)$, to the cooling rate by IR emission, i.e.,

$$H_{coll}(a, n, T) = 4\pi a^2 \int \pi B_\nu(T_d)Q_\nu(a)\, d\nu \equiv 4\pi a^2 \sigma_B T_d^4 \langle Q(a, T_d)\rangle . \tag{3}$$

Here, $B_\nu(T_d)$ is the Planck function, σ_B is the Stephan-Boltzmann constant, and $Q_\nu(a)$ is the dust emissivity. Values for $Q_\nu(a)$ were calculated from the theory, using the optical constants of Draine (1981) and Draine & Lee (1984). $\langle Q(a, T_d)\rangle$ is the Planck-averaged value of $Q_\nu(a)$, and T_d is the equilibrium dust temperature. For a given grain size, we thus obtain the heating rate from equation (2), and the equilibrium dust temperature from the right-hand side of equation (3). Reinserting this into the middle term of equation (3) yields the emitted spectrum as a function of wavelength. Integration over the distribution of grain sizes finally gives the overall IR emission spectrum.

2.3. *Grain Sputtering*

To obtain grain thermal sputtering rates, define Y to be the particle sputtering yield, or the average number of particles released from the grain per collision (cf. Dwek & Arendt 1992). The value of Y is calculated via the formalism of Anderson & Bay (1981) and Bohdansky (1984) and is a function of incident particle and energy, the mass and nuclear charge of the sputtered atoms, and their binding energy to the dust. For graphite, C atoms of mass 12 m_H are assumed to be the yield. For the silicates, we assume that molecules similar to $MgSiFeO_4$ comprise the grains, and the sputtered atoms have average mass 23 m_H. All atoms released from the grains are assumed to be neutral. We refer the reader to Tielens et al. (1994) and Dwek et al. (1994) for a complete discussion of these calculations. Inserting $\xi = Y$ into equation (2) and integrating yields the rate at which atoms are liberated as a function of grain type, grain velocity, particle type, and particle temperature.

General trends indicate that because Y is independent of grain radius, the change in grain radius as a function of time, da/dt, is independent of size. Silicates, due to higher sputtering

© American Astronomical Society • Provided by the NASA Astrophysics Data System

1994ApJ...431..188V

yield, are generally destroyed faster than their graphite counterparts. For all grains, the sputtering rate increases with temperature until $\sim 10^8$ K, at which point the grains begin to become transparent to the incoming particles. Whereas electrons are dominant in grain heating, protons and He nuclei are primarily responsible for destroying the dust. The main effect of grain motion is to increase the sputtering rate at lower temperatures, due in part to the additional energy per collision available to overcome the binding potential.

2.4. *Grain Dynamics*

It is important to follow dust trajectories in the postshock region accurately, since we wish to predict IR and X-ray emissions as a function of postshock distance. Immediately behind the shock front, the grains move ballistically, streaming through the postshock gas at a relative velocity of 3/4 V_s. However, they eventually get caught up in the postshock flow and come to rest as they are slowed and destroyed by collisions with the postshock gas. (We emphasize that our nomenclature assumes the reference frame of the shock front. Observers in the rest frame of the preshock gas will see the dust accelerated by collisions with postshock constituents.)

There are several forces which effectively couple the grain to the gas. These include simple collisions, Coulombic forces for charged grains (Draine & Salpeter 1979; Shull 1978), and gyromotion of charged grains about magnetic field lines (Shull 1977; Spitzer 1978). These processes become more effective in the recombination zones of radiative shocks, where enhanced densities and magnetic fields accelerate the dust and increase the rate of grain-grain collisions.

At the temperature and densities considered here, the grain charge is well known, and not much dependent on the interstellar radiation field. To a very good approximation, we can take the grain potential $\phi = 0$ (McKee et al. 1987). This negates the effects of Coulomb and gyromagnetic forces and diminishes the role of magnetic fields, which neither affect neutral grains nor play a meaningful role in nonradiative shock structure. Thus, we need consider only the grain drag force due to direct collisions. We define $\xi = mv \cos\theta$, insert into equation (1), and sum over all plasma constituents to obtain the rate of momentum transfer to the grains. This, coupled with the mass of the grain, yields the deceleration rate as a function of radius.

We furthermore believe that the detailed study of neutral grains is warranted as the foundation for future efforts, since potential uncertainties in grain charging and the magnitude and orientation of local B and E fields can lead to large variations in predicted grain evolution. For the nonradiative shocks we are considering, the inclusion of grain charging and magnetic fields will have the greatest impact for small grains. The smallest grains tightly spiral about magnetic field lines in a region close to the shock front, while the motion of larger grains, by virtue of a larger radius of gyration, will more closely approximate that of the present study. Observationally, this should lead to little change in expected IR 60 μm and 100 μm emissions (which arise from larger grains) but may lead to premature enhancement of X-ray emissivities, as the smallest grains are destroyed in death spirals further upstream. A more detailed study of the effects of grain charging will appear in Dwek et al. (1994).

In previous work (Vancura 1992), we have studied the extreme cases of (1) complete decoupling between dust and plasma—grains move ballistically with no deceleration in the postshock region, and (2) complete coupling between dust and plasma—grains shocked and immersed, at rest, in the postshock plasma. We note that the results presented in the present work (incorporating grain deceleration) are in agreement with expectations in that observables initially agree with the ballistic case, but gradually approach those of grains at rest as coupling slows the grains.

2.5. *Other Assumptions*

We assume that the dust has homogeneous composition and is distributed homogeneously in the preshock gas. Elements depleted from the gas phase are bound into either bare graphite or bare silicate grains. Graphite grains are made up entirely of C and have density 2.2 g cm^{-3}. The silicate grains contain the rest of the refractory (depleted) elements and have an assumed density of 3.3 g cm^{-3}. We have chosen the initial abundances and depletions summarized in Table 1 based on previous compilations (Mathis 1990; Itoh 1989; Savage & Mathis 1979). We assume that each sputtered silicate "particle" contains the elements [O, Mg, Si, Fe, N, S, Ca] in approximately the ratio [4, 1, 1, 1, 1.5, 0.25, 0.06]. From the homogeneity of the grains, it follows that the liberation rate of depleted elements is in direct proportion to the fraction of grain volume sputtered. Metals released from the grains are assumed to be neutral.

We have adopted the distribution of grain populations first suggested by Mathis, Rumpl, & Nordsieck (1977), where the number of grains N (cm^{-3}) of radius a (μm) in a parcel of interstellar gas is given by

$$\frac{dN}{da} = ka^{-\alpha}, \tag{4}$$

for some α between limiting grain sizes a_{max} and a_{min}. Here, k is a normalization factor to be determined by equating the initial mass of depleted abundances per unit gas volume to the integrated mass of grains per unit volume. We adopt the same size distribution parameters for each type of grain. Mathis et al., in matching the 2160 Å extinction bump, found best-fit values of $\alpha = 3.5$ and $a_{max} = 0.25$ μm. We choose $a_{min} = 0.0003$ μm (Itoh 1989; Draine & Anderson 1985; Dwek & Arendt 1992).

The timescale in which ions and electrons come to equilibrium behind the shock front remains unclear. Raymond et al. (1983) favored Coulomb equilibration for a nonradiative

TABLE 1

INITIAL ABUNDANCES AND DEPLETIONS

Element	Z[a]	Depletion[b]
He	10.93	0.0
C	7.82	0.8
N	7.66	0.5
O	8.72	0.2
Ne	7.92	0.0
Mg	6.22	0.95
Si	6.25	0.95
S	6.90	0.5
Ar	6.70	0.0
Ca	4.60	0.98
Fe	5.80	0.98
Ni	6.30	0.0

[a] Log (initial abundance by number) on the scale where Z(H) = 12.00.

[b] Fractional depletion (by number) assumed in initial abundances.

© American Astronomical Society • Provided by the NASA Astrophysics Data System

1994ApJ...431..188V

filament in the NE Cygnus Loop. However, improved optical echelle data of this filament (Hester, Raymond, & Blair 1994) coupled with recent HUT observations of this region are in better agreement with models employing instant equilibration (Long et al. 1992). In this study we will treat the timescale of ion-electron temperature equilibration as a free parameter.

By assuming an equilibrium grain temperature, we have ignored the effects of stochastic heating, which occurs in small grains that undergo infrequent collisions. In this case, the proper treatment of the evolution requires a time dependent solution (Dwek 1986; Dwek et al. 1994). The effect on the 60 μm and 100 μm fluxes should be small, since these emissions arise primarily from larger grains. At the stage where the grains are almost completely destroyed, stochastic heating does contribute to the 60 μm and 100 μm emissions, but by this point the contribution is negligible. On the other hand, the implications of stochastic heating are substantial for small grain emissions at wavelengths $\lesssim 30$ μm (Dwek 1986). Therefore, in the following sections, we do not predict or consider *IRAS* 12 μm or 25 μm bandpass fluxes. However, in the following discussion, the total IR cooling rate is *always* applicable, as it is merely equal to the grain heating rate.

Finally, because we wish to predict the emission from nonradiative shocks where thermal sputtering dominates, we do not attempt to calculate grain-grain collision rates which become dominant as the gas cools and compresses. We are therefore required to truncate the shock models before significant compression has occurred. However, for a SNR blast wave still in the adiabatic phase of evolution (e.g., the primary shock in the Cygnus Loop), this limitation is not important.

3. RESULTS

We first discuss in some detail the output for conditions presently appropriate for the main blast wave in the Cygnus Loop. We then vary preshock density and shock velocity and discuss the resulting changes in output. For the Cygnus Loop model, we adopt a shock velocity of 400 km s^{-1} and a preshock density of 0.1 cm^{-3}. These values are similar to those derived by Ku et al. (1984) using *Einstein* X-ray observations of the Cygnus Loop. We truncate the shock with the onset of significant cooling at a swept-up column density (N_H) of 6×10^{19} cm^{-2}. At this point, the gas has relaxed to a temperature of 5×10^5 K, and the compression is a factor of ~ 20. We present the density and temperature distribution within the postshock flow in Figure 1. The density (0.4 cm^{-3}) and temperature (2×10^6 K) remain roughly constant until a shocked column of 10^{19} cm^{-2}. After this point, the cooling increases, with the accompanying density rise and temperature decline maintaining approximate pressure equilibrium. The present swept-up column density in the Cygnus Loop is $\sim 6 \times 10^{18}$ cm^{-2}.

The amount of sputtering, Δa, as a function of N_H is shown in Figure 2. Grains are completely destroyed when $|\Delta a| = a_{gr}$. At any given column density, the change in radius for silicates is about 70% greater than that for graphite grains. Since the sputtering rate is proportional to particle density, Δa is proportional to the swept-up column density, and the plot of Δa versus N_H is independent of preshock density.

At any point in the postshock flow, the percentage of initial grain volume still intact represents the fraction of initially depleted material still locked-up in the dust. In Figure 3, we present the fraction of grain mass remaining as a function of column density. The fraction of dust destroyed becomes sizable

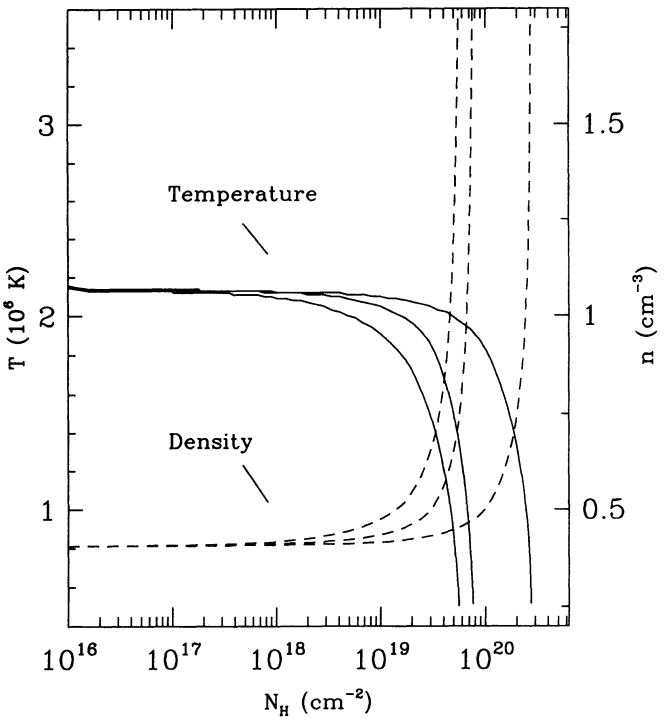

FIG. 1.—Temperature and density profile behind a 400 km s^{-1} shock with preshock density 0.1 cm^{-3}. Note the uniformity of temperature and density until a column density of $\sim 10^{19}$ cm^{-2}, after which significant cooling and compression begins. The curves are (*left to right*) (1) initially depleted abundances with grain evolution, (2) cosmic abundances with no grains, and (3) depleted abundances with no grains.

at a column density of $\sim 10^{18}$ cm^{-2}, corresponding to an age (for this model) of 8,000 yr and a linear distance of 3 pc. Only after a column density of 6×10^{18} cm^{-2} ($\sim$50,000 yr!) is roughly half the initial mass of dust destroyed.

The assumption of Coulomb equilibration has little effect on the sputtering and mass curves of Figures 2 and 3. Coulomb equilibration initially leaves the postshock "heavies" (which are responsible for most of the grain destruction) with higher temperatures than in the instant equilibration case. However, for $T \geq 10^6$ K, the sputtering rate is almost constant with temperature, which leads to a negligible difference in the two cases.

Grain destruction, by increasing the gas phase metal abundances, has the primary effect of increasing the X-ray flux from the shock. In Figures 4*a* and 4*b*, we show the 0.1–4.0 keV emissions and integrated fluxes, respectively, from the shock with instant equilibration as a function of column density. (Because the postshock temperature for a 400 km s^{-1} shock peaks near 2×10^6 K, the emission in the 0.1–2.0 keV *ROSAT* band is the same.) The X-ray flux is calculated in the usual manner as the line integral of the emission. The fluxes displayed in figures throughout this paper represent emission through the front of the shock (one-half the total emission). The top and bottom curves (*dotted lines*) represent the X-ray emission for cosmic and depleted abundances, respectively, without grain evolution. The solid curve shows the X-ray emission with the depleted initial abundances of Table 1 and grain evolution. The initial rise corresponds to the ionization timescale of ions which have strong X-ray emission lines. The subsequent gentle decline is due to ionization of elements such as

© American Astronomical Society • Provided by the NASA Astrophysics Data System

1994ApJ...431..188V

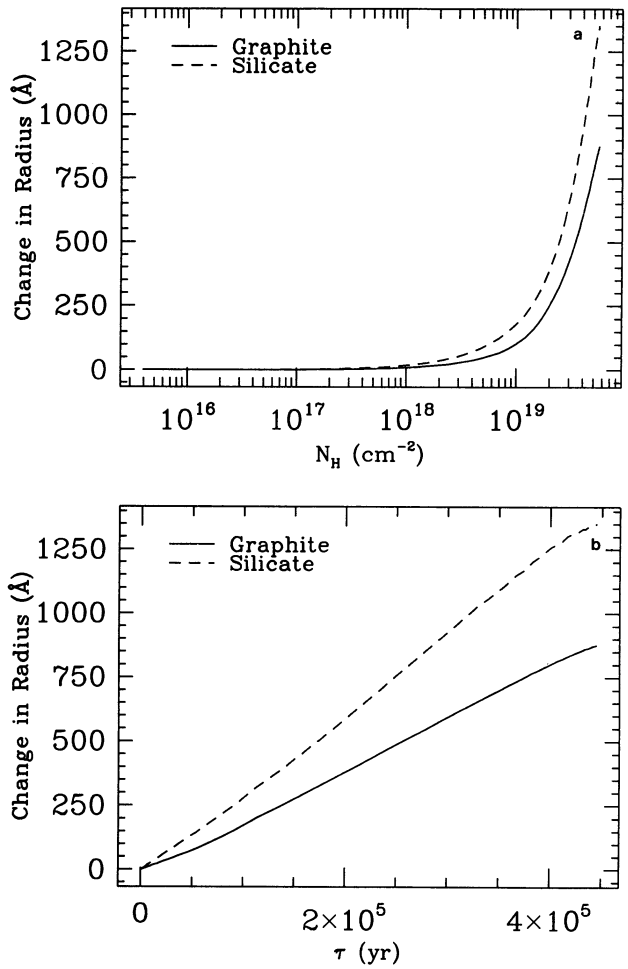

FIG. 2.—Change in radius of the grains in the postshock flow is presented (*a*) as a function of swept-up column density and (*b*) as a function of time for a 400 km s^{-1} shock with preshock density 0.1 cm^{-3}. Solid and dashed curves represent graphite and silicate grains, respectively.

Ne, Si, and Fe beyond the ions which have strong 0.25 keV lines with high excitation rates. The final upturn is due to the increase in gas phase abundances, hence cooling rate.

The X-ray emissivity is primarily a function of the metal abundance and ionization state of the gas; thus for the same temperature we would expect the cosmic abundance curve to lie above that for depleted abundances. The factor of two difference between these curves is primarily a function of the depletions that we have assumed in Table 1. At very low swept-up columns ($N_H \leq 10^{17}$ cm^{-2}) the grains are almost entirely intact; thus the X-ray emission is very close to the depleted case. As the shock evolves, the grains are gradually destroyed and the X-ray emissivity gradually departs from the depleted case. After a swept-up column density of $\sim 10^{19}$ cm^{-2}, enhanced abundances cause the cooling to become significant for the cosmic abundance and grain destruction shocks. This causes additional compression and a corresponding density rise, leading to the upturn of emission in Figure 4*a*. Notice that the model including grain evolution turns up *earlier* because of the additional energy loss due to grain heating (see below). Until this point, the local density at a given swept-up column density is roughly the same for each curve, hence the ratio of the emission curves represents the ratio of emissivities.

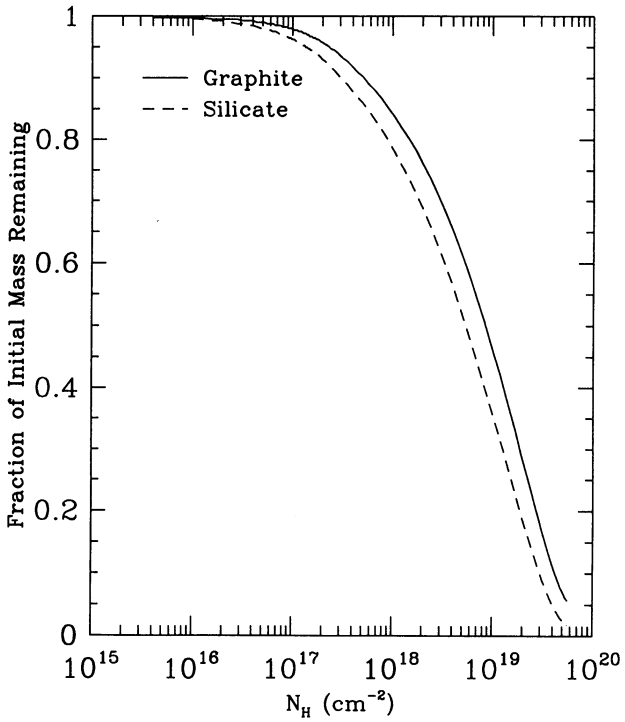

FIG. 3.—Fraction of initial mass of grains remaining as a function of swept-up column density for a 400 km s^{-1} shock with preshock density 0.1 cm^{-3}. Solid and dashed curves represent graphite and silicate grains, respectively.

Though total X-ray emission changes by only 50% or so, the *shape* of the emitted X-ray spectrum changes considerably, depending on abundances and grain evolution. This is a result of the fact that the elements suffer a wide range of initial depletions. For a plasma of temperature 2×10^6 K, most of the emission between 0.1 and 0.5 keV is dominated by high-ionization Si and Fe, while the emission harder than 0.5 keV consists mostly of O and Ne lines. Because Si and Fe are much more heavily depleted than O and Ne (see Table 1), considerable changes occur in the emitted spectrum as a function of N_H. In Figure 5 we present the integrated X-ray spectrum, passed through the *ROSAT* PSPC response, for two values of swept-up column density, N_H. In Figure 5*a*, at an N_H of 2.0×10^{17} cm^{-2}, the X-ray emission still closely resembles that of the depleted case. Notice the excess of soft emission due to excess Si and Fe line emission in the cosmic spectrum. In Figure 5*b*, with $N_H = 5.8 \times 10^{18}$ cm^{-2}, the dusty shock wave model lies between the depleted and cosmic cases. Neither abundance set excluding grain evolution can adequately represent the grain model. In particular, the depleted abundance model without grain evolution predicts an X-ray spectrum that is too hard, whereas the cosmic abundance model has too much soft X-ray emission.

The same trends in terms of total X-ray flux and X-ray spectral features are observed if we assume Coulomb equilibration of the postshock plasma. In this case, due to lower electron temperatures, the spectra are all softer. Until the ions and electrons reach equilibrium, the total X-ray flux is also less. We note that at the present swept-up column of the Cygnus Loop, even assuming Coulomb equilibration, ions and electrons have reached temperature equilibrium. The expected X-ray fluxes are virtually identical regardless of the mechanism of ion-electron equilibration except at the very edge of the SNR ($\sim 1'$).

© American Astronomical Society • Provided by the NASA Astrophysics Data System

1994ApJ...431..188V

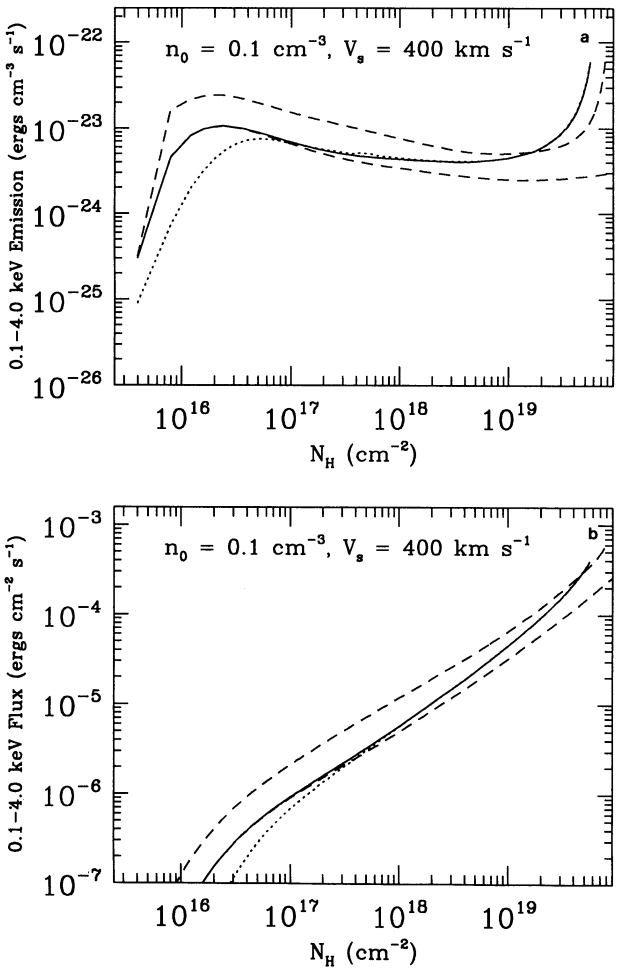

FIG. 4.—0.1–4.0 keV X-ray (*a*) emissions and (*b*) fluxes for a 400 km s^{-1} shock with preshock density 0.1 cm^{-3} and instant equilibration. The dashed curves correspond to cosmic preshock gas (*top*) and the depletions of Table 1 with no grain destruction (*bottom*). The solid curve is the model prediction incorporating initially depleted abundances and grains. Also shown for comparison as the dotted curve is the grain evolution X-ray curve employing Coulomb equilibration.

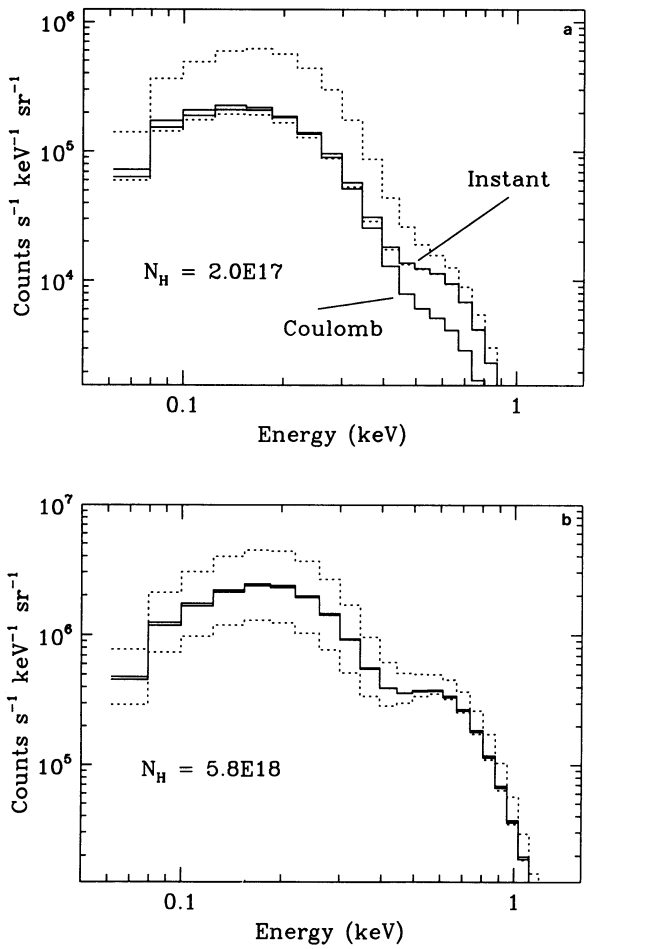

FIG. 5.—X-ray spectrum as seen by *ROSAT* PSPC for 400 km s^{-1} shock with preshock density 0.1 cm^{-3} at a swept-up column of (*a*) 2.0 × 10^{17} cm^{-2} and (*b*) 5.8 × 10^{18} cm^{-2}. The dashed curves represent cosmic (*upper*) and depleted (*lower*) abundances with no grain evolution. The solid curves represent grain evolution with instant (*upper*) and Coulomb (*lower*) equilibration. At early times the X-ray spectrum including grain evolution resembles the depleted case. However, at the present shocked column of the Cygnus Loop, either abundance set without grain evolution is incapable of reproducing the (presumed) actual case.

We turn next to the IR emissions from the grains, which, as we shall see, comprise the greatest energy loss mechanism in the postshock wave region. Figure 6 shows the predicted IR emissions and fluxes for this shock as a function of column density for the case of instant equilibration. The dashed and dotted curves represent emission through the 60 μm and 100 μm *IRAS* bandpasses, respectively, while the solid curves represent the entire IR emissions due to grain heating. Initially when most of the grains are intact, the silicate emissions are greater by a factor of two due to a greater heating rate. However, because the silicates are sputtered away faster, the graphite emissions rise relative to the silicates at larger column densities, and the graphite emission eventually exceeds that of the silicates for $N_H \geq 10^{18}$ cm^{-2}. Until $\sim 10^{18}$ cm^{-2}, because the grains are mostly intact, the IR emissions rise slowly due to grain deceleration (compression of the grain "fluid"), and the integrated fluxes rise almost linearly. After this point, with the onset of substantial obliteration of the grains, the emission curves fall, appearing as a flattening of the integrated flux.

As expected, the assumption of Coulomb equilibration affects only the predicted IR emissions for young shocks. As depicted in Figure 7, after the swept-up column density exceeds $\sim 4 \times 10^{17}$ cm^{-2}, there is no appreciable difference in IR emissions between the two cases of equilibration, for after this point, the ions and electrons are at equal temperatures. The difference in emissions at small N_H is primarily due to the lower electron temperatures in the Coulomb case. Note that at the present swept-up column of 6×10^{18} cm^{-2}, the mechanism of equilibration is irrelevant to IR emissions, as was the case for X-ray emissions.

Varying the preshock density has predictable effects on the X-ray emissions. We have run additional models for a 400 km s^{-1} shock in a preshock density of 0.01 and 1.0 cm^{-3}. The Δa and mass sputtered curves (Figs. 2 and 3) remain identical to the 0.1 cm^{-3} density case, as mentioned above. Thus, as a function of swept-up column density, the emissivity of the X-ray gas will remain the same. The new X-ray emission curves may be obtained by scaling the vertical axis of Figure 4*a* by

© American Astronomical Society • Provided by the NASA Astrophysics Data System

1994ApJ...431..188V

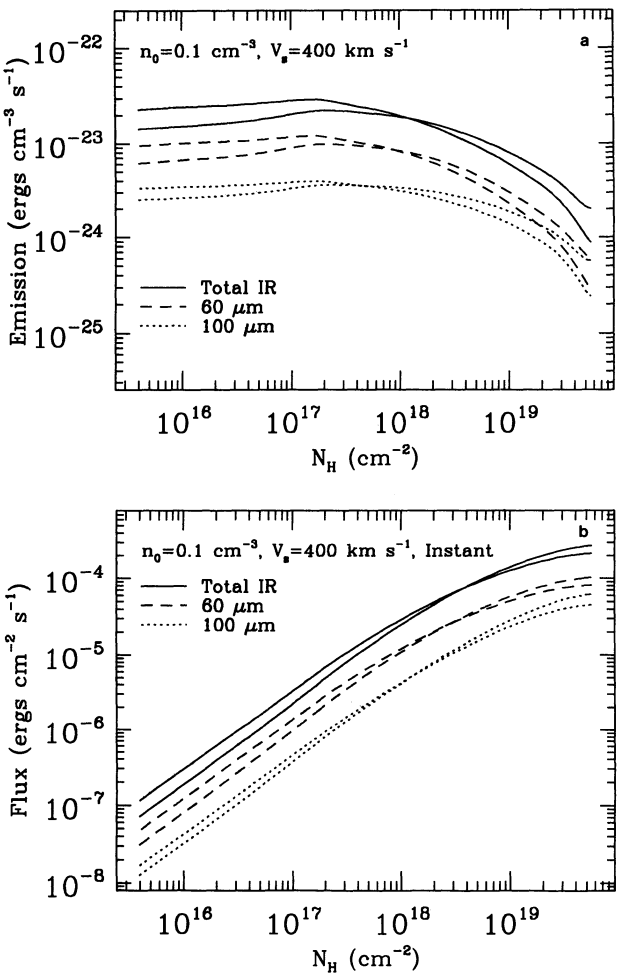

FIG. 6.—IR emission from grains for a 400 km s^{-1} shock with preshock density 0.1 cm^{-3} and instant equilibration. The IR (*a*) emissions and (*b*) fluxes are presented as a function of swept-up column density. The solid, dash, and dotted curves correspond to total IR emission, emission through the 60 μm *IRAS* bandpass, and emission through the 100 μm *IRAS* bandpass, respectively. In each case, the upper curve represents emission from silicate grains, and the lower from graphite.

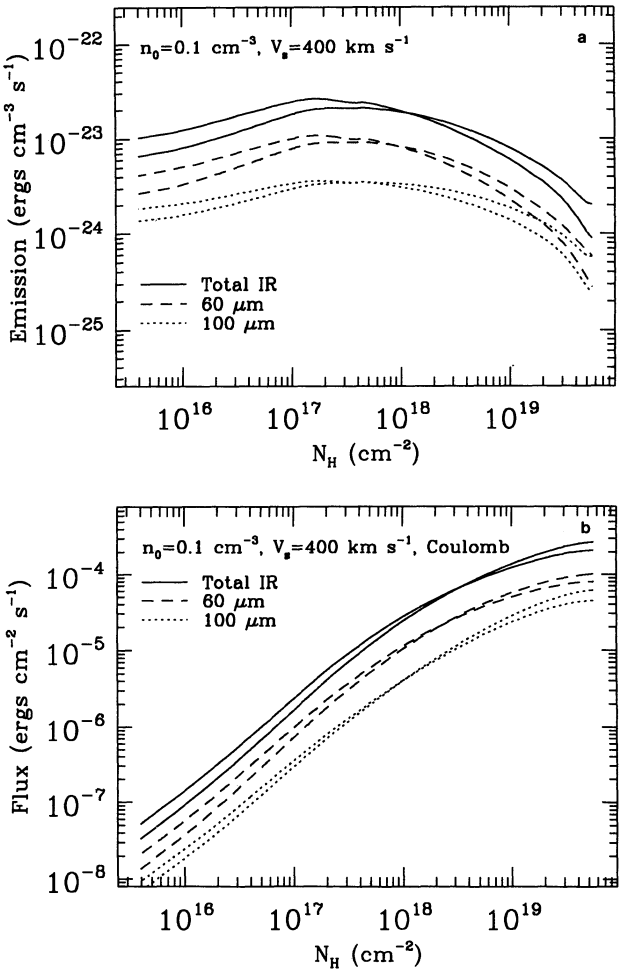

FIG. 7.—IR emission from grains for a 400 km s^{-1} shock with preshock density 0.1 cm^{-3} and Coulomb equilibration. The IR (*a*) emissions and (*b*) fluxes are presented as a function of swept-up column density. The solid, dash, and dotted curves correspond to total IR emission, emission through the 60 μm *IRAS* bandpass, and emission through the 100 μm *IRAS* bandpass, respectively. In each case, the upper curve represents emission from silicate grains, and the lower from graphite.

$(n/0.1)^2$. Similarly, the X-ray fluxes for other densities are obtained by scaling the vertical axis of Figure 4*b* by $n/0.1$.

On the other hand, the IR bandpass fluxes are somewhat sensitive to preshock density. In Figure 8 we present the postshock IR grain fluxes from 400 km s^{-1} shocks in preshock densities of 0.01 cm^{-3}, 0.1 cm^{-3}, and 1.0 cm^{-3}. As expected, the *total* IR emission scales linearly with preshock density. However, inspection reveals that as the density increases, the ratio of fluxes in the 60 μm and 100 μm *IRAS* bandpasses, $I(60):I(100)$, increases. For instance, at a column density of 6×10^{18} cm^{-2}, the ratio is equal to 0.9 for $n = 0.01$ cm^{-3} but rises to 4.8 for $n = 1$ cm^{-3}. The ratio $I(\text{IR total}):I(100)$ increases also, from 3.5 to 12.9, under the same conditions. These trends occur because, for a given grain radius, the heating rate ($\propto n$) increases the equilibrium grain temperature ($\propto n^{0.15}$; Dwek 1987), which in turn shifts the emission spectrum to shorter wavelengths.

To explore changes in output as a function of shock velocity, we have also run models at 300, 700, 1000, and 1500 km s^{-1} with a preshock density of 0.1 cm^{-3}. Figure 9 demonstrates how the rate of grain destruction changes, with the mass fraction remaining plotted as a function of swept-up column density. In all cases, the curves lie in a narrow range. However, the observed trend (with N_H) is that the fraction of volume remaining first falls and then rises with increasing shock velocity, which can be understood as follows. As the shock velocity increases from 300 km s^{-1} (postshock $T = 1.3 \times 10^6$ K) to 700 km s^{-1} ($T = 6.9 \times 10^6$ K), the sputtering rate is increased (see Dwek et al. 1994). This is countered by the shorter propagation time (for a given N_H) for the 700 km s^{-1} shock. However, the increased sputtering rate dominates the two effects to yield the observed trend. Increasing the velocity further to 1500 km s^{-1} ($T = 3.2 \times 10^7$ K), has little further effect on the sputtering rate. Consequently, the continually shorter time of evolution (with increasing shock velocity) yields a greater fraction of dust volume remaining intact.

The variation of X-ray spectral hardness with shock velocity (hence, temperature) is well understood. Here, we will simply present another example of how grain evolution modifies the emergent X-ray spectrum. In Figure 10, we have taken the

© American Astronomical Society • Provided by the NASA Astrophysics Data System

1994ApJ...431..188V

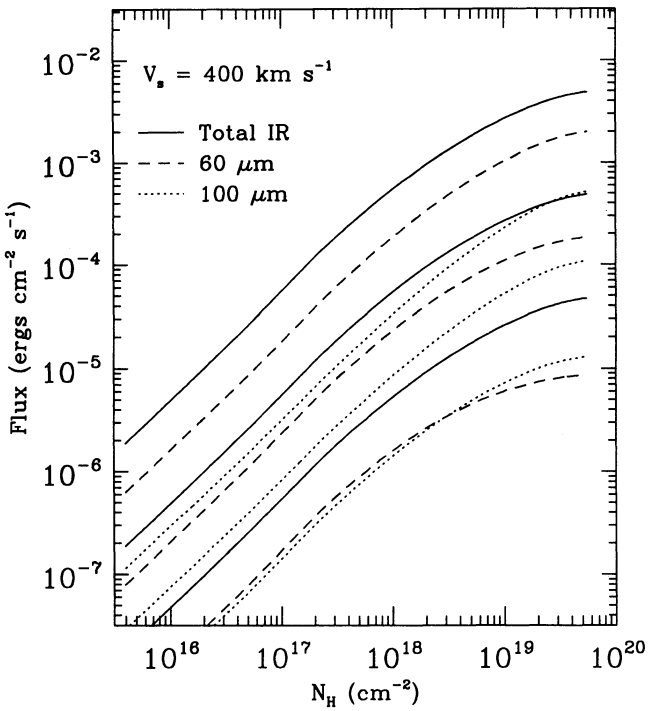

FIG. 8.—Comparison of IR fluxes from a 400 km s^{-1} shock with different preshock densities. The contributions from both graphite and silicate dust have been summed. The solid curves correspond to total IR grain emissions for preshock densities of 0.01 cm^{-3} (*lowest*), 0.1 cm^{-3} (*middle*), and 1 cm^{-3} (*top*). The set of dash curves corresponds to the same sequence of densities for the 60 μm *IRAS* bandpass, while the dotted curves represent emission through the 100 μm *IRAS* bandpass. Notice that the ratio of $I(60):I(100)$ and I(IR total):$I(100)$ increases as the preshock density rises.

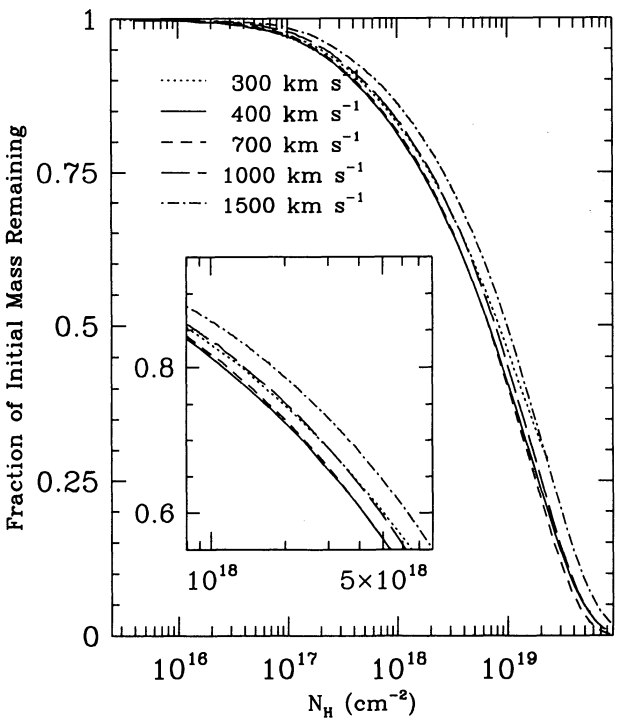

FIG. 9.—Grain mass curves for different shock velocities. The curves represent fraction of mass remaining for different shock speeds. Notice that all curves lie in a narrow band.

integrated X-ray spectrum of the 1500 km s^{-1} shocks described above and passed them through the response of the ASCA SIS aboard *Astro-D*. We present spectra at two differing swept-up columns, the first being indicative of present conditions in SN 1006 (Vartanian, Lum, & Ku 1984; Hamilton, Sarazin, & Szymkowiak 1986). In the present epoch, the grain case approximates an X-ray gas with depleted abundances and is at great odds with the cosmic abundance model. At later times the grain evolution solution will differ considerably from either abundance set excluding grains. For reference, in the Coulomb interaction case, full temperature equilibration between ions and electrons does not occur until $N_H = 9 \times 10^{19}$ cm^{-2}.

The predicted IR fluxes for the shocks with different velocities are portrayed in Figures 11–15, and several conclusions may be drawn. The IR fluxes rise with increasing velocity due to increased heating. A shock velocity increase tends to slightly increase I(60):I(100) and I(IR total):I(100) because of the corresponding postshock temperature rise. Shocks greater than 500 km s^{-1} will completely destroy the preshock grain population before the shock becomes radiative.

Our modeling indicates that grain heating is the dominant energy loss mechanism for the postshock gas and plays a vital role in the timescale for transition to a shock becoming radiative. The IR:X-ray ratio thus serves as an important indicator in determining energy losses and evolutionary properties of a shock wave. In Figures 16*a* and 16*b*, we present the predicted I(IR total):I(X-ray >0.1 keV) ratio for the various shocks we have considered herein. Because the total IR and X-ray fluxes each scale linearly with density, the corresponding IR:X-ray curves remain valid independent of preshock density. The IR:X-ray ratio typically falls between 1 and 100.

4. COMPARISON TO CYGNUS LOOP OBSERVATIONS

The Cygnus Loop has been studied extensively in the far IR, where most of the emission arises from heated dust. Braun & Strom (1986) found the *IRAS* emission to be shell-like and similar in morphology to X-ray and optical emissions. Arendt, Dwek, & Leisawitz (1992) decomposed the *IRAS* emission from the Cygnus Loop into distinct X-ray–related and optical-related components. The X-ray–related component occurs as the grains are collisionally heated in the postshock flow of the main blast wave and reflected bow shocks. The optical-related component arises from radiatively and collisionally heated dust in the cooling flow of radiative shocks where there is also a contribution from IR line emission. Our predictions should be directly comparable to the X-ray component.

For the collisionally heated component that is spatially correlated with the X-ray gas, Arendt et al. (1992) find flux levels for the entire SNR of roughly 1650 and 2940 Jy at 60 μm and 100 μm, respectively, with an uncertainty of ~20%. This corresponds to fluxes of 4.4×10^{-8} and 2.9×10^{-8} ergs cm^{-2} s^{-1}, in the 60 μm and 100 μm bandpasses. The total 0.1–4.0 keV X-ray flux from the Cygnus Loop is $\sim 1.6 \times 10^{-8}$ ergs cm^{-2} s^{-1} (Ku et al. 1984). Arendt et al. (1992) have separated the Cygnus Loop into several smaller regions and calculated IR and X-ray fluxes for each. These regions show IR–to–X-ray ratios of 0.4–3.8 for the 60 μm band and 0.2–5.4 for the 100 μm band. Ratios of the fluxes in the two bands, $I(60):I(100)$, range from roughly 0.5 to 2.2, with $I(60) > I(100)$ at most positions. X-ray regions that are also optically bright (implying locations where the blast wave has encountered large clouds) exhibit

© American Astronomical Society • Provided by the NASA Astrophysics Data System

1994ApJ...431..188V

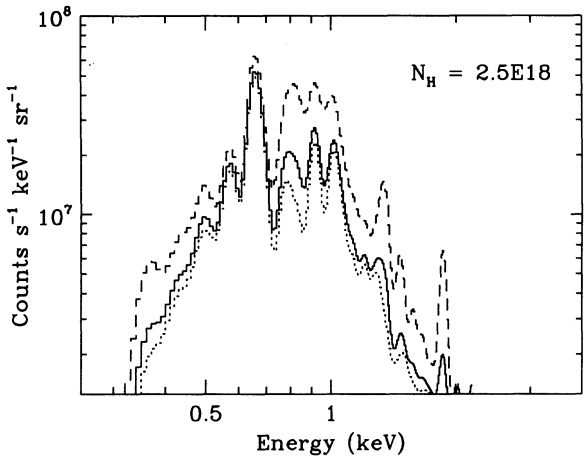

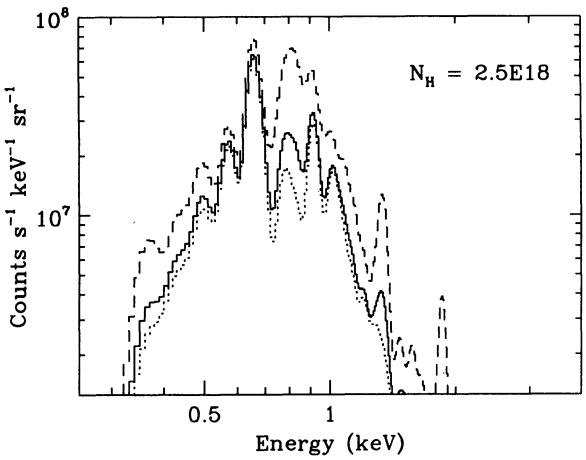

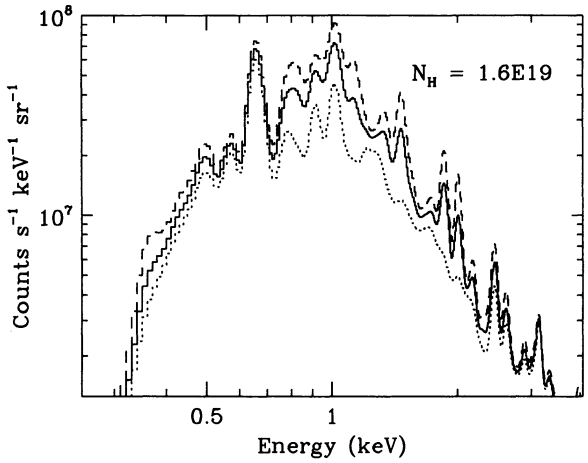

FIG. 10*a*

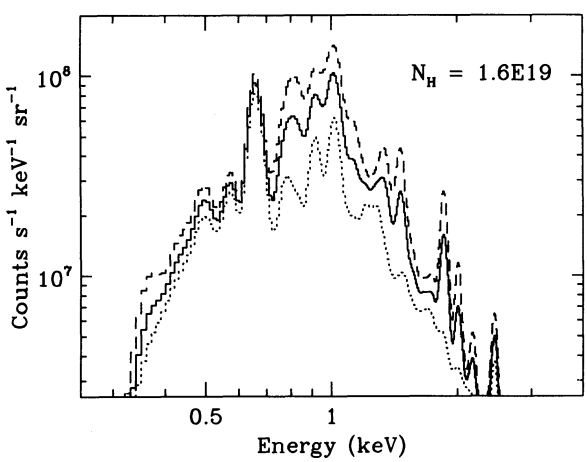

FIG. 10*b*

FIG. 10.—X-ray spectrum as seen by ASCA SIS for 1500 km s^{-1} shock with preshock density 0.1 cm^{-3}, assuming (*a*) instant and (*b*) Coulomb equilibration, at a swept-up column of 2.5 × 10^{18} cm^{-2} (*upper*) and 1.6 × 10^{19} cm^{-2} (*lower*). The upper panels are indicative of present shocked columns in SN 1006. The assumption of cosmic abundances in the X-ray plasma is clearly not valid. The lower panel shows the shock at a later epoch. At this point, neither abundance set without grain evolution can reproduce the spectrum that includes grains.

ratios which differ little from those associated with the blast wave proper.

It is not straightforward to compare the IR and X-ray data of the entire Cygnus Loop to our models. Major contributions to the X-ray emission are post–blast wave gas and X-ray enhancements associated with optical emission. We now discuss limitations in the comparison of each of these contributors to our models. First, our code does not presently account for the deceleration of the blast wave with time. So comparisons with the blast wave proper must not be overinterpreted. The Sedov (1959) solution for an explosion in a uniform density medium yields $V_b \propto R_b^{-3/2}$, where V_b and R_b are, respectively, the velocity and radius of the blast wave. Ku et al. (1984) used the X-ray observations to derive a *present* blast wave velocity of 400 km s^{-1} for a radius of ~19 pc. This would make the velocity ~1000 km s^{-1} when the radius was 10 pc. Before this, the volume of swept-up matter was only one-eighth of that today, so its effect should be small on the present observed flux. The *absolute* fluxes in the IR and X-ray are a sensitive function of the history of the blast wave velocity. However, from the above discussion the relative $I(60):I(100)$ ratio is not, so for the present purposes of a ratio comparison, a steady state shock will suffice. The proper analysis including a Sedov solution will appear in a future paper. Second, the brightest X-ray emission arises in overpressured regions encompassed by reverse bow shocks, where the blast wave has encountered large clouds. The gas entering the reverse shock is already comprised of post–blast wave material. However, the post–blast wave time is sufficiently small that we may assume the grains are still almost entirely intact upon entering the reverse shock. To first order, the effect of the reverse shock is to maintain an overpressured region, compared to the continuous relaxation of pressure with a Sedov solution. In the northeast Cygnus Loop, for example, Hester et al. (1994) estimate a present swept-up column density of 1.3 × 10^8 cm^{-2} for the reverse shock. Hester et al. further conclude that pressure equilibrium will be maintained until $N_H \approx 5 \times 10^{18}$ cm^{-2}. Thus, for reverse shocks, the assumption of a steady state shock of 400 km s^{-1} is probably appropriate, although the preshock density and shocked column may be larger than that associated with the blast wave proper. With these caveats in mind, values for $I(60):I(100)$ for the shock velocities discussed in § 3

© American Astronomical Society • Provided by the NASA Astrophysics Data System

1994ApJ...431..188V

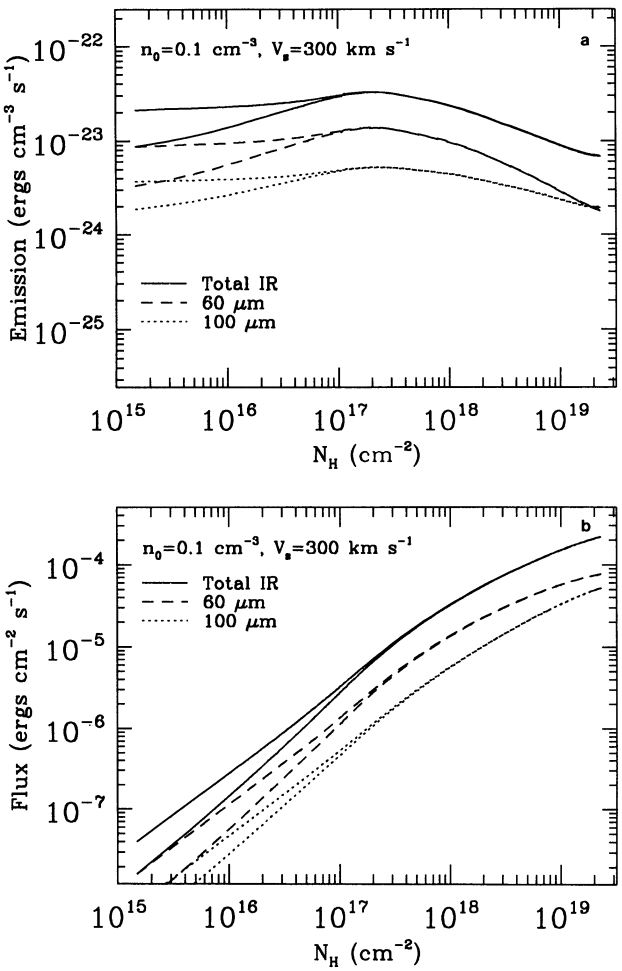

FIG. 11.—IR emission from grains for a shock velocity of 300 km s^{-1}. (*a*) The solid, dash, and dotted curves represent total, 60 μm bandpass, and 100 μm bandpass IR emissions, respectively, for a shock speed of 300 km s^{-1}, assuming instant (*upper*) and Coulomb (*lower*) equilibration. (*b*) Same as (*a*) for flux through the shock front.

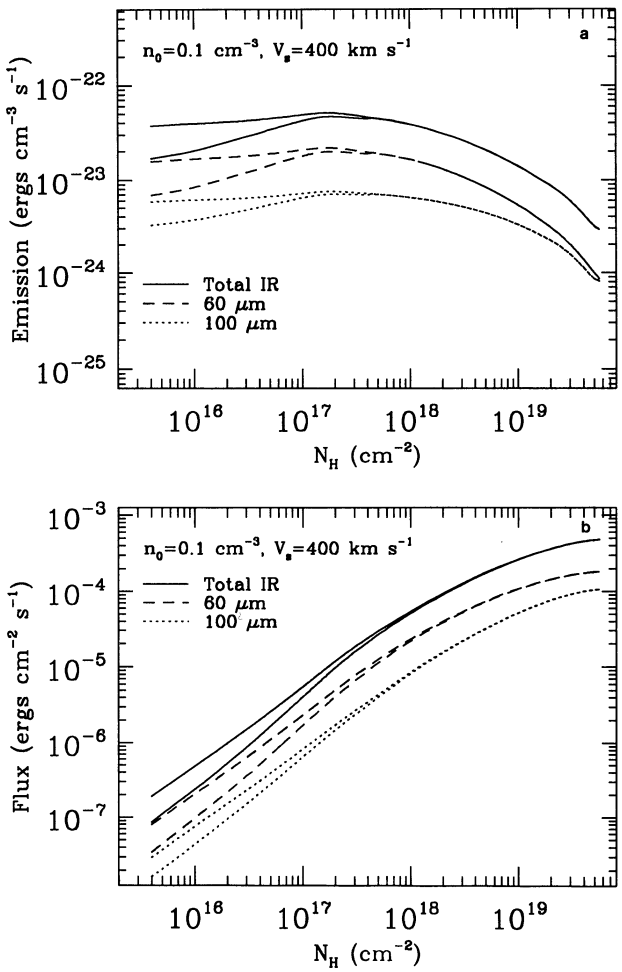

FIG. 12.—IR emission from grains for a shock velocity of 400 km s^{-1}. Same as Fig. 11 for a shock of 400 km s^{-1}.

range from ~2 to 4 at a present swept-up column of 1–6 × 10^{18} cm^{-2}. This range is only slightly greater than the observed global ratio of ~1.5.

Spatial regions closer to the primary shock front permit a more detailed analysis. The *IRAS* spatial resolution is roughly 3′ (Neugebauer et al. 1984), while that of the *Einstein* IPC is about 2′ (cf. Ku et al. 1984). Two arcminutes at the distance of the Cygnus Loop (770 pc) corresponds to a linear distance of ~0.5 pc. With the blast wave parameters of the Cygnus Loop, this distance corresponds to a swept-up column density of ~7 × 10^{17} cm^{-2}, with this gas being shocked ~2 pc further inward. Since this time the blast wave velocity has remained constant to within 15% (30% for a linear distance of 1 pc), so the approximation that the blast wave is represented by a steady state 400 km s^{-1} shock wave is reasonable.

We overplot the expected IR and X-ray fluxes from a shock with $V_s = 400$ km s^{-1} and $n_0 = 0.1$ cm^{-3} in Figure 17. At a column of ~10^{18} cm^{-2} the predicted flux ratio $I(60):I(100):I(X)$ is roughly 4.0:1.5:1, which is in reasonable agreement with the observations (0.4–3.8:0.2–5.4:1) for individual regions in the Cygnus Loop (Arendt et al. 1992). Absolute values of observed fluxes in the IR and X-ray are also reproduced by assuming the blast wave to cover the surface of a 19 pc sphere, although this may be somewhat fortuitous given the discussion above.

We predict several other diagnostics for the dust presently engulfed by the main blast wave of the Cygnus Loop. The dust furthest behind the primary shock front has had sputtering decrease its volume to ~55% of the initial value. Typical changes in radii due to sputtering for these furthest grains are between 50 and 100 Å. Assuming a 400 km s^{-1} shock with preshock density 0.1 cm^{-3}, our gain temperatures at the present swept-up column density of the Cygnus Loop range from ~25 K for the large grains to ~50 K for the smallest sizes. This is in good accord with the derived color temperature of ~31 K (Arendt et al. 1992) for the IR emission associated with the X-ray shell.

5. RAMIFICATIONS

To date, most IR analyses of SNRs have been made assuming that grains are immersed in steady state plasmas. The distribution of grain sizes, dust-to-gas ratio, gas temperature, and gas density are then adjusted to match the observations. Inspection of Figure 1 reveals that until a column of

© American Astronomical Society • Provided by the NASA Astrophysics Data System

1994ApJ...431..188V

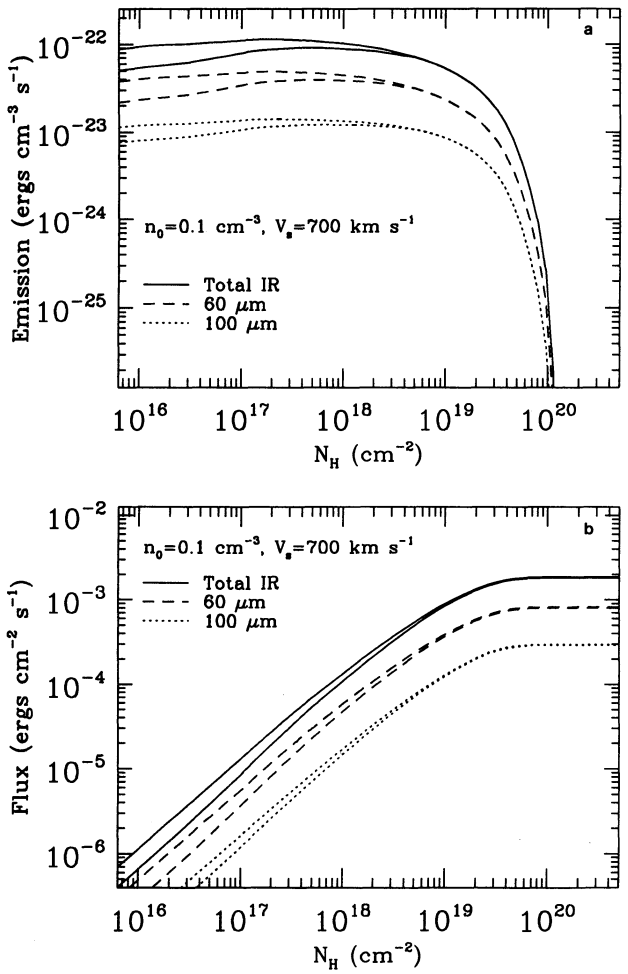

FIG. 13.—IR emission from grains for a shock velocity of 700 km s^{-1}. Same as Fig. 11 for a shock of 700 km s^{-1}.

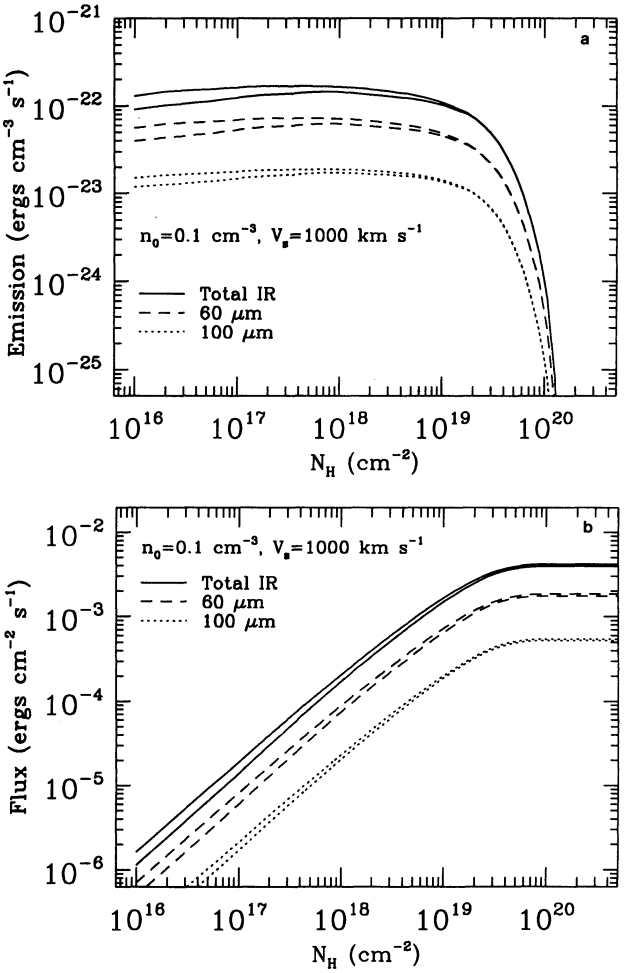

FIG. 14.—IR emission from grains for a shock velocity of 1000 km s^{-1}. Same as Fig. 11 for a shock of 1000 km s^{-1}.

roughly 10^{19} cm^{-2}, the shocked gas can, with a high degree of accuracy, be treated simply as a plasma of density 0.4 cm^{-3} and temperature 2×10^6 K. Indeed, further indication of this is seen in Figure 2*b*, from which it is clear that the change in grain radius as a function of time is constant even for column depths $> 10^{19}$ cm^{-2} where cooling sets in. It is evident that the emission decline of Figure 12, beginning at a column density of 4×10^{17} cm^{-2}, is occurring because the grains are being destroyed, as opposed to changes in the physical state of the plasma. Thus, the X-ray study of stationary grains in high temperature plasmas by Itoh (1988) is quantitatively similar to that presented herein. The differences can be ascribed to our treatment of grain deceleration through the postshock fluid.

With the abundances and depletions that we have assumed, the difference in X-ray emission between any two of the models in Figure 8 is at most a factor of 2, which given a volume and luminosity, corresponds to an error of $\sim$40% in the derived density of the gas.

The shape of the X-ray spectrum is important in determining temperatures. In single temperature spectral fitting, we estimate the error in derived temperature to be 25%–40% in assuming either a depleted or cosmic abundance set and excluding grain evolution. In particular, assuming cosmic abundances will yield a derived temperature too high by 25%. This correlates to an implied error of roughly 10%–15% in the present blast wave velocity. Because Ku et al. (1984) assumed cosmic abundances and a single temperature, we conjecture that the present blast wave velocity in the Cygnus Loop may actually be closer to 350 km s^{-1}. If this is the case, the SNR may be older, preshock density higher, or explosion energy less than previously thought. Whether or not a shell has been recently encountered, the remnant may be closer to becoming radiative than generally believed. Due to the long timescale for grain destruction in the hot X-ray gas (see Fig. 9), we believe depleted abundances are the most appropriate foundation for further X-ray spectral studies of SNRs. However, an appropriate depleted abundance set for each target remains problematic. In principle, by observing the X-ray spectrum of a fast shock at several points in the postshock region, we expect that differential spectra could be used to derive improved estimates of initial depletions.

Grain evolution in the postshock flow potentially "stretches" out the zone of line emissions of several atomic species. In a pure plasma shock wave, atoms are quickly ionized to equilibrium values, and lines of intermediate and low ionization species are emitted in a thin region near the shock front. However, with grain evolution, neutral atoms of heavily depleted species are continually being released into the postshock plasma by the sputtering of grains. Thus, the zones of emission of several important diagnostics such as C III λ977,

© American Astronomical Society • Provided by the NASA Astrophysics Data System

1994ApJ...431..188V

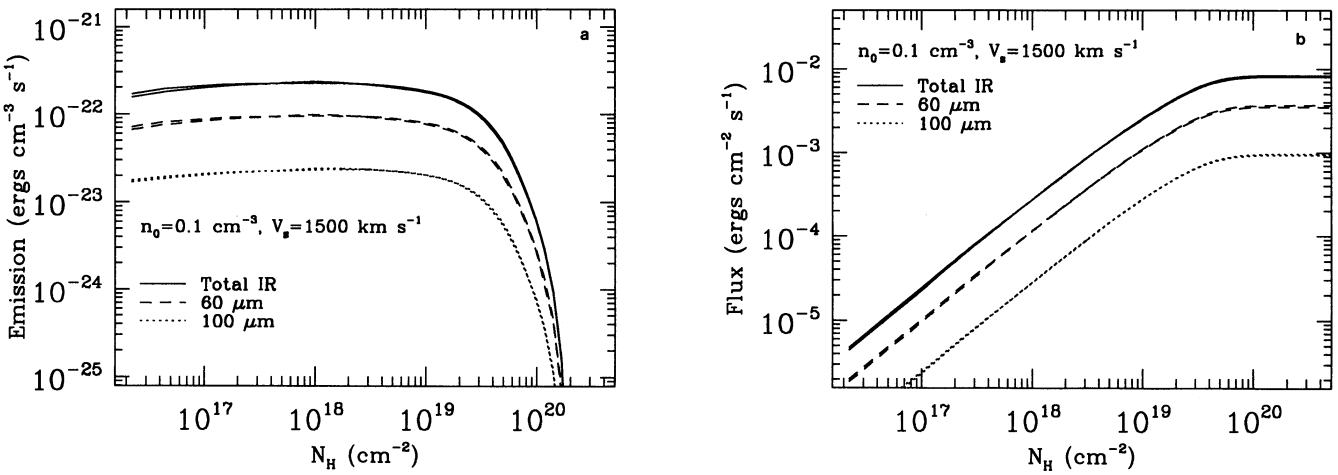

FIG. 15.—IR emission from grains for a shock velocity of 1500 km s^{-1}. Same as Fig. 11 for a shock of 1500 km s^{-1}.

C IV λ1550, Si III] λ1892, [Fe X] λ6573, and [Fe XIV] λ5303 among others, may become extended and the morphology of these line emissions may not be as abrupt as previously thought. This may have implications for the interpretation of spectral imaging studies.

In the UV, key diagnostic lines include S VI λ939, O VI λ1035, N V λ1240, and C IV; of these, we expect the "stretching" of line emission to be most dramatic for C IV, due to the greatest depletion of C among the elements C, N, O, and S. We have run our code to study this effect for a 400 km s^{-1} shock with preshock density 0.1 cm^{-3}, as per § 4. Our modeling indicates that, for depleted abundances without grain evolution, the fluxes through the front of the shock for S VI, O VI, N V, and C IV, are 6.8×10^{-9}, 9.7×10^{-7}, 4.5×10^{-8}, and 3.5×10^{-8} ergs cm^{-2} s^{-1}, respectively at a column of $\sim 6 \times 10^{16}$ cm^{-2}. After this point the postshock plasma has ionized beyond the point where further emission in these lines occurs. Further substantial emission in these lines does not occur until $N_H \geq 2.0 \times 10^{18}$ cm^{-2}. However, by allowing grain evolution (and the continual release of neutral atoms into the gas phase), we

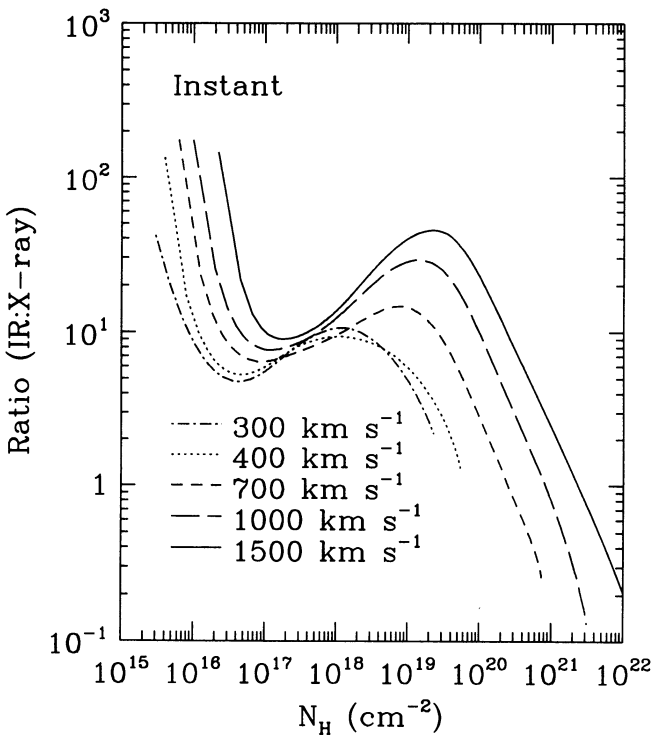

FIG. 16a

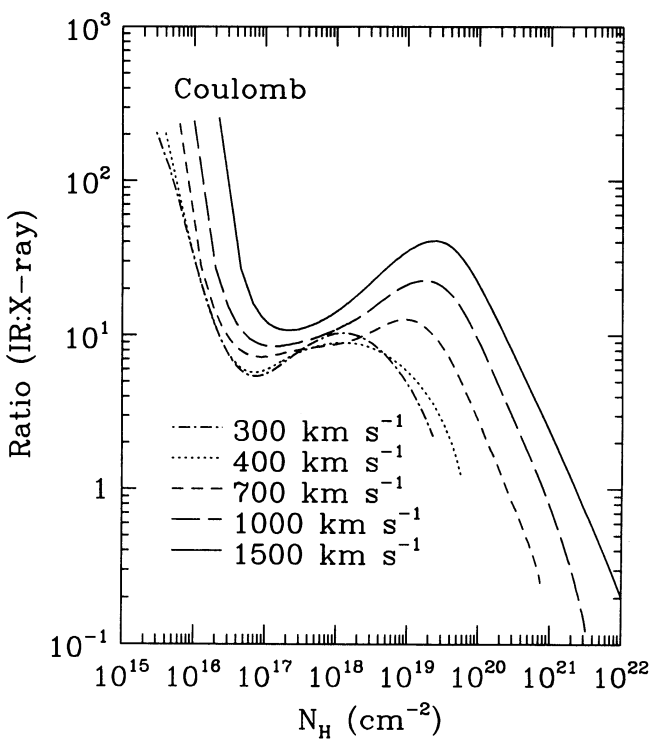

FIG. 16b

FIG. 16.—IR:X-ray ratio for various shock velocities assuming (*a*) instant or (*b*) Coulomb equilibration. The curves are independent of preshock density and represent the ratio of total IR (= grain heating) to total X-ray (>0.1 keV) fluxes. Typical values for the ratio are 1 to 100 and verify that dust heating is the dominant energy loss mechanism for the postshock plasma.

© American Astronomical Society • Provided by the NASA Astrophysics Data System

1994ApJ...431..188V

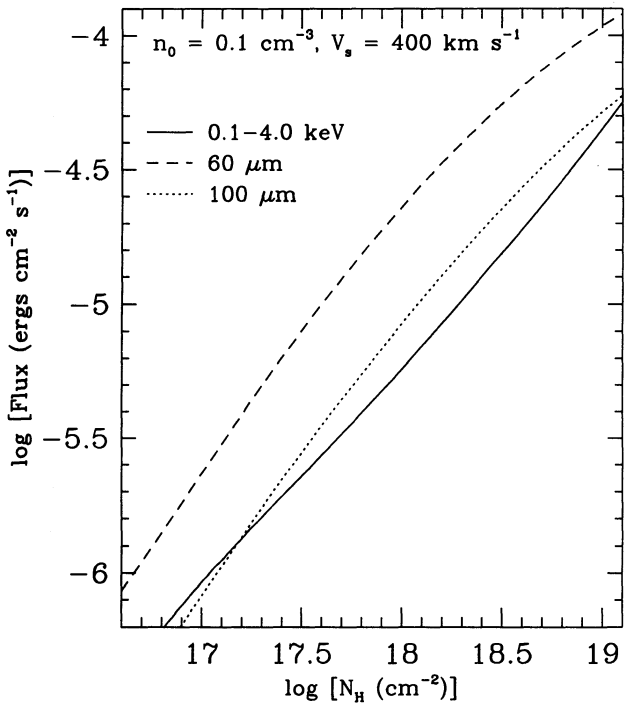

FIG. 17.—IR and X-ray fluxes for a shock of velocity 400 km s^{-1} with preshock density 0.1 cm^{-3}. The solid curve represents 0.1–4.0 keV X-ray flux. The dash curve represents 60 μm *IRAS* bandpass integrated flux for grains, while the dotted curve represents the 100 μm *IRAS* flux.

find that the emissions in these lines will continue past 6×10^{16} cm^{-2}. For example, we find, at $N_H = 1.0 \times 10^{18}$, that the fluxes are 1.0×10^{-8}, 1.4×10^{-6}, 7.6×10^{-8}, and 7.6×10^{-8} ergs cm^{-2} s^{-1}, respectively, if grain evolution is included. The emissivity of each line in the "stretched" zone is far less than in the initial shock front region but remains roughly constant (and nonzero) due to continual grain destruction. For example, the emissivity of the C IV line is $\sim 2 \times 10^{-25}$ ergs cm^3 in the "stretched" zone.

6. CONCLUSIONS

We have constructed models that predict the dynamic evolution and emission of grains behind nonradiative shock waves. We have incorporated thermal sputtering, heating, and deceleration of grains in the postshock flow, and we have predicted the associated IR grain and X-ray plasma fluxes as a function of swept-up column density. We have studied the effects of varying preshock density and shock velocity on X-ray and IR emissions.

For the X-ray gas, we find that the depletions we have assumed may lead to a factor of 2 difference in absolute X-ray fluxes, if we consider cases with and without grain evolution. This corresponds to errors of 40% in density determinations. Furthermore, by ignoring grains in the postshock flow, we estimate an error of 25%–40% in temperature determinations based on the shape of the X-ray spectrum. This leads to errors of 10%–20% in velocity determinations. We suggest that future X-ray studies of SNRs should adopt depleted abundances as their basis.

The total IR flux from the grains rises linearly with n_0, and IR emissions also rise with increasing shock velocity. At greater postshock temperatures, the larger grain heating rate implies higher grain temperatures, which decreases the value of the 100 μm flux relative to the 60 μm and total IR fluxes. We have presented theoretical IR:X-ray ratio curves for various shock velocities as a function of shock column density. Values for the IR:X-ray ratio typically range from 1 to 100.

We have modeled grain destruction behind shocks with conditions applicable to the main blast wave in the Cygnus Loop. The results agree with the IR and X-ray fluxes reported by Arendt et al. (1992). Our models agree with observed *IRAS* and X-ray fluxes, IR–to–X-ray ratios, and total luminosities from the SNR. This agreement with the observations on both absolute and relative scales is encouraging. Based on X-ray spectra and IR line ratios, we believe that the blast wave velocity is probably less than the canonical 400 km s^{-1}.

Our investigations of the large parameter space of this problem are ongoing. In particular, in the context of IR and X-ray emissions, we are making modifications to study nonzero grain potentials and stochastic heating (Dwek et al. 1994). We are studying the effects of different grain composition and size distributions. Finally, we are modifying the shock code in order to more accurately represent a decelerating blast wave.

This project was supported by NASA grants NAG 5-2453 to The Smithsonian Astrophysical Observatory and NAG 5-1793 to The Johns Hopkins University, and by NASA Infrared Astrophysics (Code EZ) RTOP No. 188-44-53-05.

REFERENCES

Anderson, H. H., & Bay, H. L. 1981, in Sputtering by Particle Bombardment I, ed. R. Behrisch (Berlin: Springer-Verlag), 145
Arendt, R. G., Dwek, E., & Leisawitz, D. 1992, ApJ, 400, 562
Bohdansky, J. 1984, Nuclear Instr. Meth. Phys. Res., B2, 587
Braun, R., & Strom, R. G. 1986, A&A, 164, 208
Cox, D. P., & Raymond, J. C. 1985, ApJ, 298, 651
Draine, B. T. 1981, ApJ, 245, 880
Draine, B. T., & Anderson, N. 1985, ApJ, 292, 494
Draine, B. T., & Lee, H. M. 1984, ApJ, 285, 89
Draine, B. T., & Salpeter, E. E. 1979, ApJ, 231, 77
Dwek, E. 1986, ApJ, 302, 363
———. 1987, ApJ, 322, 812
Dwek, E., & Arendt, R. G. 1992, ARA&A, 30
Dwek, E., Foster, S., Vancura, O., & Raymond, J. C. 1994, in preparation
Hamilton, A. J. S., Sarazin, C. L., & Szymkowiak, A. E. 1986, ApJ, 300, 698
Hester, J. J., Raymond, J. C., & Blair, W. P. 1994, ApJ, 420, 721
Itoh, H. 1989, PASJ, 41, 853
Ku, W. H.-M., Kahn, S. M., Pisarski, R., & Long, K. S. 1984, ApJ, 278, 615
Long, K. S., Blair, W. P., Vancura, O., Bowers, C. W., Davidsen, A. F., & Raymond, J. C. 1992, ApJ, 400, 214
Mathis, J. S. 1990, ARA&A, 28, 37
Mathis, J. S., Rumpl, W., & Nordsieck, K. H. 1977, ApJ, 217, 425
McKee, C. F., Hollenbach, D. J., Seab, C. G., & Tielens, A. G. G. M. 1987, ApJ, 318, 674
Neugebauer, G., et al. 1984, ApJ, 278, L1
Raymond, J. C. 1979, ApJS, 39, 1
Raymond, J. C., Blair, W. P., Fesen, R. A., & Gull, T. R. 1983, ApJ, 275, 636
Savage, B. D., & Mathis, J. S. 1979, ARA&A, 17, 73
Seab, C. G. 1987, in Interstellar Processes, ed. D. J. Hollenbach & H. A. Thronson, Jr. (Dordrecht: Reidel), 491
Sedov, L. I. 1959, Similarity and Dimensional Methods in Mechanics (New York: Academic)
Shull, J. M. 1977, ApJ, 215, 805
———. 1978, ApJ, 226, 858
Spitzer, L. 1978, Physical Processes in the Interstellar Medium (New York: John Wiley & Sons)
Tielens, A. G. G. M., McKee, C. F., Seab, C. G., & Hollenbach, D. J. 1994, in ApJ, 431, 000
Vancura, O. 1992, Ph.D. thesis, The Johns Hopkins University
Vartanian, M. H., Lum, K. S. K., & Ku, W. H.-M. 1984, ApJ, 288, L5

© American Astronomical Society • Provided by the NASA Astrophysics Data System